



OPEN ACCESS

EDITED BY

Steve Suib,
University of Connecticut, United States

REVIEWED BY

Yuichi Kitagawa,
Hokkaido University, Japan
Ashis K. Patra,
Indian Institute of Technology Kanpur, India

*CORRESPONDENCE

Jouliia Larionova,
✉ jouliia.larionova@umontpellier.fr
Alexey N. Bilyachenko,
✉ bilyachenko@ineos.ac.ru
Albano N. Carneiro Neto,
✉ albanoneto@ua.pt

RECEIVED 31 January 2024

ACCEPTED 07 March 2024

PUBLISHED 03 April 2024

CITATION

Félix G. Kulakova AN, Sene S, Khrustalev VN, Hernández-Rodríguez MA, Shubina ES, Pelluau T, Carlos LD, Guari Y, Carneiro Neto AN, Bilyachenko AN and Larionova J (2024), Luminescent Ln³⁺-based silsesquioxanes with a β-diketonate antenna ligand: toward the design of efficient temperature sensors. *Front. Chem.* 12:1379587. doi: 10.3389/fchem.2024.1379587

COPYRIGHT

© 2024 Félix, Kulakova, Sene, Khrustalev, Hernández-Rodríguez, Shubina, Pelluau, Carlos, Guari, Carneiro Neto, Bilyachenko and Larionova. This is an open-access article distributed under the terms of the [Creative Commons Attribution License \(CC BY\)](https://creativecommons.org/licenses/by/4.0/). The use, distribution or reproduction in other forums is permitted, provided the original author(s) and the copyright owner(s) are credited and that the original publication in this journal is cited, in accordance with accepted academic practice. No use, distribution or reproduction is permitted which does not comply with these terms.

Luminescent Ln³⁺-based silsesquioxanes with a β-diketonate antenna ligand: toward the design of efficient temperature sensors

Gautier Félix¹, Alena N. Kulakova^{1,2}, Saad Sene¹, Victor N. Khrustalev^{3,4}, Miguel A. Hernández-Rodríguez^{5,6}, Elena S. Shubina², Tristan Pelluau¹, Luís D. Carlos⁵, Yannick Guari¹, Albano N. Carneiro Neto^{5*}, Alexey N. Bilyachenko^{2,3*} and Jouliia Larionova^{1*}

¹CNRS, ENSCM, University Montpellier, Montpellier, France, ²Nesmeyanov Institute of Organoelement Compounds, Russian Academy of Sciences, Moscow, Russia, ³Peoples' Friendship University of Russia (RUDN University), Moscow, Russia, ⁴Zelinsky Institute of Organic Chemistry, Russian Academy of Sciences, Moscow, Russia, ⁵Phantom-g, Physics Department and CICECO—Aveiro Institute of Materials, University of Aveiro, Aveiro, Portugal, ⁶Departamento de Física, Universidad de La Laguna San Cristóbal de La Laguna, Santa Cruz de Tenerife, Spain

We report the synthesis and single-crystal X-ray diffraction, magnetic, and luminescence measurements of a novel family of luminescent cage-like tetranuclear silsesquioxanes (PhSiO_{1.5})₈(LnO_{1.5})₄(O)(C₅H₈O₂)₆(EtOH)₂(CH₃CN)₂·2CH₃CN (where Ln = Tb, **1**; Tb/Eu, **2**; and Gd, **3**), featuring seven-coordinated lanthanide ions arranged in a one-capped trigonal prism geometry. Compounds **1** and **2** exhibit characteristic Tb³⁺ and Tb³⁺/Eu³⁺-related emissions, respectively, sensitized by the chelating antenna acetylacetonate (acac) ligands upon excitation in the UV and visible spectral regions. Compound **3** is used to assess the energies of the triplet states of the acac ligand. For compound **1**, theoretical calculations on the intramolecular energy transfer and multiphonon rates indicate a thermal balance between the ⁵D₄ Stark components, while the mixed Tb³⁺/Eu³⁺ analog **2**, with a Tb:Eu ratio of 3:1, showcases intra-cluster Tb³⁺-to-Eu³⁺ energy transfer, calculated theoretically as a function of temperature. By utilizing the intensity ratio between the ⁵D₄→⁷F₅ (Tb³⁺) and ⁵D₀→⁷F₂ (Eu³⁺) transitions in the range 11–373 K, we demonstrate the realization of a ratiometric luminescent thermometer with compound **2**, operating in the range 11–373 K with a maximum relative sensitivity of 2.0% K⁻¹ at 373 K. These findings highlight the potential of cage-like silsesquioxanes as versatile materials for optical sensing-enabled applications.

KEYWORDS

thermometry, silsesquioxanes, lanthanides, luminescence, magnetism, energy transfer

1 Introduction

Luminescent coordination complexes containing trivalent lanthanide ions (Ln³⁺) have attracted significant attention over several decades due to tremendous perspectives in different applications, including bioimaging and biosensing (Eliseeva and Bünzli, 2009; Ning et al., 2019), light-emitting technology (Bünzli, 2019; Costa et al., 2024), smart

windows (Choi et al., 2017; Fernandes et al., 2018; Costa et al., 2024), nano-thermometry (Allison, 2019; Brites et al., 2019; Brites et al., 2023), detection of molecules and ions (Eliseeva and Bünzli, 2009; Allison, 2019; Brites et al., 2023), cell labeling (Aulsebrook et al., 2018; Bodman and Butler, 2021). These compounds exhibit distinctive photophysical characteristics, manifesting as prolonged emission with lifetimes extending up to milliseconds. This extended emission attributed to the $4f-4f$ transitions occurs in the visible and/or near-infrared (NIR) spectral domains depending on the nature of the Ln^{3+} ion. Moreover, it usually includes narrow emission lines, significant ligand-induced Stokes shifts, and high quantum yields. For these reasons, the coordination chemistry of Ln^{3+} ions employed in association with various ligands to design mono- and polynuclear compounds of various topologies with optimized optical properties has been the subject of huge development during recent decades (Bünzli, 2010; Bünzli, 2015; SeethaLekshmi et al., 2017; Liu et al., 2020; Monteiro, 2020; Bernot et al., 2021). In particular, extensive effort has been focused on the synthesis of highly luminescent, photo- and thermostable complexes valuable for the above-mentioned applications (Kaczmarek et al., 2019).

However, directly exciting the $4f$ levels poses a challenge as the majority of the $f-f$ transitions are prohibited by the Laporte rule, resulting in low molar absorption coefficients. This constraint can be surmounted by the tune of organic chromophores as ligands to generate the well-known “antenna effect,” yielding highly emissive complexes. In these systems, chromophore ligands, typically excited in the UV or, less frequently, in the visible spectral domains, allow the energy transfer from the ligand triplet excited state to the emitting level of the Ln^{3+} ion. Consequently, this process induces a radiative decay in the visible or NIR spectral regions depending on the Ln^{3+} ion used (Bünzli, 2015). Note that an alternative mechanism has been documented, which entails the energy transfer from the first excited singlet state of the ligand to the $4f$ levels (Alaoui, 1995; Yang et al., 2004; Kasprzycka et al., 2017; Gregório et al., 2019; Moura Jr. et al., 2021a; Manzur et al., 2023). Hence, achieving efficient energy transfer requires a meticulous alignment of energy levels and adherence to selection rules among various excited states. This optimization can be accomplished through a careful selection of ligands and Ln^{3+} ions, coupled with the strategic design of the metal center geometry within a suitable ligand environment (Carneiro Neto et al., 2019). Furthermore, note that improved luminescence has been documented in complexes featuring an asymmetric Ln^{3+} coordination environment, notably in a seven-coordinated geometry (Miyata et al., 2009; Miyata et al., 2012; Yanagisawa et al., 2015; Ferreira da Rosa et al., 2020; Aquino LE do et al., 2021).

A significant breakthrough in Ln^{3+} -based luminescent coordination compounds lies in their application as temperature sensors, enabling remote temperature measurements through emission monitoring. This approach offers temperature sensing with high spatial precision (below $10\ \mu\text{m}$), temporal (time scale) and thermal resolutions ($0.1\ \text{K}$) within short acquisition times (less than $10\ \mu\text{s}$), and high relative thermal sensitivity ($S_r > 1\% \text{K}^{-1}$) (Brites et al., 2012; Jaque and Vetrone, 2012; Brites et al., 2016; Brites et al., 2019; Brites et al., 2023). It shows enormous potential in a wide range of applications ranging from biology and medicine to cryogenics (Cui et al., 2012; Bettinelli et al., 2015; Dramićanin, 2020). Starting from the first example showing the possibility of the

real-time observation of thermogenesis in a single HeLa cell using the simple mononuclear $\text{Eu}(\text{tta})_3$ complex (where tta^- is 3-thenoyltrifluoroacetate) (Suzuki et al., 2007), numerous Ln^{3+} -based compounds have been investigated for this purpose. A particular emphasis in this field has been placed on the design of ratiometric thermometers, in which a luminescence intensity ratio (LIR) of two constituent Ln^{3+} ions is used as a signal permitting a self-referencing emissive system (Brites et al., 2010). The most used complexes contain a $\text{Tb}^{3+}/\text{Eu}^{3+}$ pair due to the high quantum yield of these ions, for which different parameters can be optimized to increase the performance of the luminescent thermometers (Cui et al., 2012; Rocha et al., 2016; Lyubov et al., 2022). In particular, molecular cluster-aggregates have shown high potential for this purpose, attributed to a rigid metal core of high nuclearity, precise coordination environment, and tunable energy transfer. This is achieved through the precise control of the ratio of the ions and the distance between them, as well as their structural organization, ion environment, and the nature of ligands (Calado et al., 2023; Gálico et al., 2023). A particular family of these molecular cluster-aggregates, luminescent Ln^{3+} -based silsesquioxanes, provides a compelling alternative to coordination complexes, offering high photothermal and chemical stabilities, particularly pertinent with increasing temperature for thermometry applications.

Cage-like Ln^{3+} -based metallasilsesquioxanes are an exciting family of compounds presenting the combination of Ln^{3+} ions with the silsesquioxane repeating subunits, $(\text{RSiO}_{1.5})_n$ (where $n = 6, 8, 10, 12, \dots$). The latter permits the construction of inorganic Si-O-Si skeletons as a basic structural unit, realizing cyclic and polycyclic types of matrixes, which offer these architectures the chemical stability, mechanical robustness, thermal stability, and possibility to form cage-like topology. Moreover, they possess oxygen atoms able to coordinate Ln^{3+} ions and, therefore, integrate and specially organize them inside the cage-like rigid framework. Moreover, terminal ligands may also be coordinated with the metal ions to complete their coordination environment, bringing additional functionalities. These architectures have mainly been investigated as molecule-based models for catalysis (Herrmann et al., 1994; Shchegolikhina et al., 1996; Annand et al., 1999; Annand and Aspinall H, 2000; Arnold et al., 2001; Lorenz et al., 2002; Lorenz et al., 2004; Wu et al., 2009; Marchesi et al., 2014; Davies et al., 2017; Sheng et al., 2022a; Sheng et al., 2022b), but recently, their magnetic (Sheng et al., 2022b) and optical properties (Sheng et al., 2022a) have also been investigated. Recently, we reported the first examples of luminescent Tb^{3+} , Eu^{3+} , and Dy^{3+} -based metallasilsesquioxanes presenting unusual (for metallasilsesquioxanes) anionic prism-like structures. These structures encompass four Ln^{3+} ions linked through oxygen atoms and situated between two cyclic tetraphenylcyclotetrasiloxanolate moieties (Kulakova et al., 2020; Kulakova et al., 2021; Nigoghossian et al., 2021; Félix et al., 2023a; Félix et al., 2023b). They present Ln^{3+} characteristic luminescence and interesting magnetic properties, depending on the nature of the ion, chemical robustness, and thermal stability. Moreover, we demonstrated that anionic cages containing mixed $\text{Tb}^{3+}/\text{Eu}^{3+}$ exhibited a tunable thermosensitive Tb^{3+} -to- Eu^{3+} energy transfer and proposed them as an efficient temperature sensor operating in the range $300\text{--}373\ \text{K}$ with good linearity and repeatability. Remarkably, these compounds presented an important stability

to photobleaching at a relatively high working temperature (100°C) due to the presence of the siloxane matrix, which played a protective role. However, the Ln³⁺ ions in these structures are not coordinated with antenna ligands, and the excitation was performed directly in the 4f levels, which is not optimal to achieve highly luminescent materials.

A major objective of the present work consists of the sensitization of Ln³⁺ luminescence in the silsesquioxane cages through the coordination of an antenna ligand. The most popular chelating acetylacetonate (*acac*) antenna has been used as a terminal ligand for this purpose (de Sá et al., 2000; Arnold et al., 2001; Eliseeva and Bünzli, 2009; Bünzli and Eliseeva, 2013; Gállico et al., 2023). Here, we report the synthesis, crystal structures, magnetic properties, and luminescence investigations of three new tetranuclear complexes (PhSiO_{1.5})₈(LnO_{1.5})₄(O)(C₅H₈O₂)₆(EtOH)₂(CH₃CN)₂·2CH₃CN (where Ln = Tb (**1**), Tb/Eu (**2**), and Gd (**3**)) by introducing a terminal chelating ligand *acac* coordinated with the Ln³⁺ ions. Notably, this not only permits to afford an antenna effect and sensitizes the characteristic 4f luminescence but also induces an important change in the geometry of the ions from distorted antiprism (octa-coordinated) to a pentagonal bipyramidal geometry (seven-coordinated), which can positively impact their photophysical properties (Ferreira da Rosa et al., 2020). Complexes **1** and **2** present high Tb³⁺ or Tb³⁺/Eu³⁺ characteristic emissions and paramagnetic properties, while complex **3** has been used to assess the energies of the triplet states of the *acac* ligand. Theoretical calculations on the intramolecular energy transfer and multiphonon rates for the Tb³⁺-based compound indicate a thermal balance between Stark components of the ⁵D₄ level. The mixed Tb³⁺/Eu³⁺ analog showcases intra-cluster Tb³⁺-to-Eu³⁺ energy transfer and may be used for efficient temperature sensing with good stability, sensibility (S_r = 2.0 % K⁻¹ at 373 K), and repeatability after several heating/cooling cycles.

2 Materials and methods

Phenyltrimethoxysilane (98%), Et₄NCl (≥98%), Eu(NO₃)₃·6H₂O (99.9% trace metal basis), Tb(NO₃)₃·6H₂O (99.9% trace metal basis), ethanol, acetylacetonate, and acetonitrile were purchased from Merck and used as received.

2.1 Synthesis

Compounds **1–3** were synthesized in a similar way. A mixture of PhSi(OMe)₃ and NaOH was dissolved in 30 mL of ethanol. The resulting solution was heated to reflux for 1.0 h. Afterward, Tb(NO₃)₃·6H₂O for compound **1** (or the mixture of Tb(NO₃)₃·6H₂O and Eu(NO₃)₃·6H₂O, in a 3:1 ratio, for compound **2**, or Gd(NO₃)₃·5H₂O for compound **3**) and sodium acetylacetonate dissolved in 30 mL of CH₃CN were added at once. The resulting mixture was heated to reflux for 3.0 h. Filtration of the mixture from the insoluble part provided a non-colored solution. Slow evaporation of solvents (ethanol/CH₃CN) provided, in 5–10 days, many crystalline materials. The single crystals suitable for single-crystal X-ray diffraction were collected. The crystal products were dried in a vacuum to perform elemental analysis and calculate the yield.

(PhSiO_{1.5})₈(TbO_{1.5})₄(O)(C₅H₈O₂)₆(EtOH)₂(CH₃CN)₂·2CH₃CN **1**. Reactant loadings: PhSi(OMe)₃ (0.186 g, 0.8 mmol), NaOH (0.032 g, 0.8 mmol), Tb(NO₃)₃·6H₂O (0.174 g, 0.4 mmol), and sodium acetylacetonate (0.049 g, 0.4 mmol). Yield = 30% (0.068 g).

Anal. calcd for C₇₈H₈₈Tb₄O₃₀Si₈: % C 39.60, % H 3.75. Found: % C 39.54, % H 3.71. IR in KBr pellets (cm⁻¹): 3443 (w), 3071 (s), 3048 (s), 1592 (s), 1519 (s), 1384 (w), 1129 (s), 1051 (w), 1027 (w), 952 (s), 945 (w), 835 (s), 745 (s), 700 (s), 676 (s), 576 (s), 547 (s), and 494 (s). (PhSiO_{1.5})₈(TbO_{1.5})₃(EuO_{1.5})₁(O)(C₅H₈O₂)₆(EtOH)₂(CH₃CN)₂·2CH₃CN **2**. Reactant loadings: PhSi(OMe)₃ (0.186 g, 0.8 mmol), NaOH (0.032 g, 0.8 mmol), Tb(NO₃)₃·6H₂O (0.131 g, 0.3 mmol), Eu(NO₃)₃·5H₂O (0.043 g, 0.1 mmol), and sodium acetylacetonate (0.049 g, 0.4 mmol). Yield = 25% (0.057 g).

Anal. calcd for C₇₈H₈₈Eu₃O₃₀Si₈Tb: % C 39.95, % H 3.78. Found: % C 39.89, % H 3.73. EDS analysis: Tb/Eu ratio 22.1/7.4. IR in KBr pellets (cm⁻¹): 3619 (s), 3365 (w), 3071 (s), 3048 (s), 1592 (s), 1518 (s), 1429 (s), 1384 (w), 1266 (s), 1129 (s), 1052 (m), 950 (s), 745 (s), 701 (s), 676 (s), 576 (s), and 494 (s).

(PhSiO_{1.5})₈(GdO_{1.5})₄(O)(C₅H₈O₂)₆(EtOH)₂(CH₃CN)₂·2CH₃CN **3**. Reactant loadings: PhSi(OMe)₃ (0.186 g, 0.8 mmol), NaOH (0.032 g, 0.8 mmol), Gd(NO₃)₃·5H₂O (0.173 g, 0.4 mmol), and sodium acetylacetonate (0.049 g, 0.4 mmol). Yield = 39% (0.092 g).

Anal. calcd for C₇₈H₈₈Gd₄O₃₀Si₈: % C 39.71, % H 3.76. Found: % C 39.63, % H 3.72. IR in KBr pellets (cm⁻¹): 3439 (w), 3066 (s), 3045 (s), 1596 (s), 1517 (s), 1390 (w), 1121 (s), 1060 (w), 1025 (w), 950 (s), 940 (w), 833 (s), 741 (s), 690 (s), 674 (s), 579 (s), 544 (s), and 491 (s).

2.2 Characterization

IR spectra (KBr pellets) were recorded using a PerkinElmer Spectrum Two FT-IR spectrometer. The quantification of Eu, Tb, and Si was performed using a scanning electron microscope and energy-dispersive X-ray analysis (SEM-EDX) on a FEI Quanta FEG 200 instrument. The powders were deposited on an adhesive carbon film and analyzed under vacuum. The heavy elements were quantified using INCA software, with a dwell time of 3 μs.

The emission and excitation spectra were at first evaluated at room (298 K) and low (77 K) temperatures using an Edinburgh FLS-920 spectrofluorimeter. The excitation source was a 450-W Xe arc lamp. The spectra were corrected for the detection and optical spectral response of the spectrofluorimeter. In the second step, the emission spectra were measured as a function of the temperature. The temperature setup included a thermal element (Heidolph, MR Hei-Tec [EU], 825 W, plate diameter 145 mm), a thermal camera (Optris PI 450i, accuracy ± 0.01°C), an excitation source, and a detector. The powder sample was placed on a cover glass (14 mm diameter) at the center of the heating source. The thermal camera was positioned at an angle of 30° relative to the sample to work as a temperature standard controller. A UV LED operating at 365 nm (Thorlabs M365L2) was used to excite the samples (I = 0.7A) by irradiating at 15 mm from the sample surface.

The spectrometric detector and the excitation source were coupled using a multimode fiber. The fiber excitation output and detector were located at the top of the sample. A long-pass filter (in-line fiber optic filter mount, Thorlabs, FOFMS/M, 450 nm, 20 μm) was placed in the light path between the sample and detector to avoid artifacts arising from the excitation source. The emission

spectra were recorded in the temperature range from 300 to 376 K. At each temperature step, 10 min was provided to allow the temperature to stabilize, and then, 10 emission spectra were recorded from an average of 10 consecutive spectra with an integration time of 100 ms.

The UV-visible-NIR absorption spectrum was measured using a Specord 210 Plus spectrophotometer (Analytik Jena AG, Germany). Magnetic susceptibility data were collected using a Quantum Design MPMS-XL SQUID magnetometer working between 1.8 and 350 K with a magnetic field up to 7 T. The sample was prepared under an ambient condition. The data were corrected for the sample holder, and the diamagnetic contributions were calculated from Pascal's constants.

2.3 Crystal structure determination

X-ray diffraction data for compounds **1–3** were collected using a three-circle Bruker D8 QUEST PHOTON-III CCD diffractometer ($\lambda(\text{MoK}\alpha)$ radiation, graphite monochromator, and φ and ω scan modes) and corrected for absorption using the SADABS program. The data were indexed and integrated using the SAINT program. Details are given in [Supplementary Table S1](#). The structures were solved by direct methods and refined by the full-matrix least squares technique on F2 with anisotropic displacement parameters for non-hydrogen atoms. The hydrogen atoms of the OH groups were localized in difference Fourier maps and refined isotropically with fixed-displacement parameters [$U_{\text{iso}}(\text{H}) = 1.5U_{\text{eq}}(\text{O})$]. The other hydrogen atoms were placed in calculated positions and refined within the riding model with fixed isotropic displacement parameters [$U_{\text{iso}}(\text{H}) = 1.5U_{\text{eq}}(\text{C})$ for the CH_3 groups and $1.2U_{\text{eq}}(\text{C})$ for the other groups]. All calculations were carried out using the SHELXTL program suite.

Crystallographic data have been deposited in the Cambridge Crystallographic Data Center, CCDC 2189837 (**1**), CCDC 2189838 (**2**), and CCDC 2189839 (**3**). Copies of this information may be obtained free of charge from the Director, CCDC, 12 Union Road, Cambridge CB2 1EZ, United Kingdom (Fax: +44 1223 336033; e-mail: deposit@ccdc.cam.ac.uk or www.ccdc.cam.ac.uk).

The crystal structure was determined in the Department of Structural Studies of Zelinsky Institute of Organic Chemistry, Moscow, Russia.

3 Results and discussion

3.1 Synthesis and crystal structures

The synthesis of Ln^{3+} -based silsesquioxanes ($\text{PhSiO}_{1.5}$)₈($\text{LnO}_{1.5}$)₄($\text{O}(\text{C}_5\text{H}_8\text{O}_2)_6(\text{EtOH})_2(\text{CH}_3\text{CN})_2$)₂ \cdot 2 CH_3CN (where Ln = Tb **1**, Tb/Eu **2**, and Gd **3**) with an antenna ligand was performed using a two-step approach involving conventional alkaline hydrolysis ([Prigyi et al., 2019](#); [Laird et al., 2021](#)) with the *in situ* formation of phenylsiloxanolate [$\text{PhSi}(\text{O})\text{ONa}$]_x species, following a self-assembling reaction with the *acac* ligand and the corresponding Ln^{3+} salts for compounds **1** (Tb^{3+}) and **3** (Gd^{3+}) or mixed Tb^{3+} and Eu^{3+} salts (with a $\text{Tb}^{3+}/\text{Eu}^{3+}$ ratio of 3/1) for compound **2**. The crystallization from an acetonitrile/ethanol

mixture affords the formation of single crystals suitable for crystallographic analysis. Single-crystal X-ray diffraction performed on compounds **1–3** indicates that they are isostructural and crystallize in the $P2_1/n$ space group ([Supplementary Table S1](#), Electronic Supplementary Material (ESI)). Their crystal packing may be viewed as an assembly of neutral tetranuclear lanthanide-based cages directed almost toward $[-1\ 1-1]$ ([Figure 1A](#) for compound **1**; [Supplementary Figures S1,S2](#), ESI for compounds **2–3**). In all compounds, the cages form layers parallel to (1 0–1). Within the layers, the cages are arranged perpendicular to each other. Two acetonitrile molecules were also crystallized in the unit cell and situated between the tetranuclear cages. The shortest intermolecular Ln–Ln distances are equal to 10.0765, 10.0709, and 10.0981 Å for compounds **1**, **2**, and **3**, respectively.

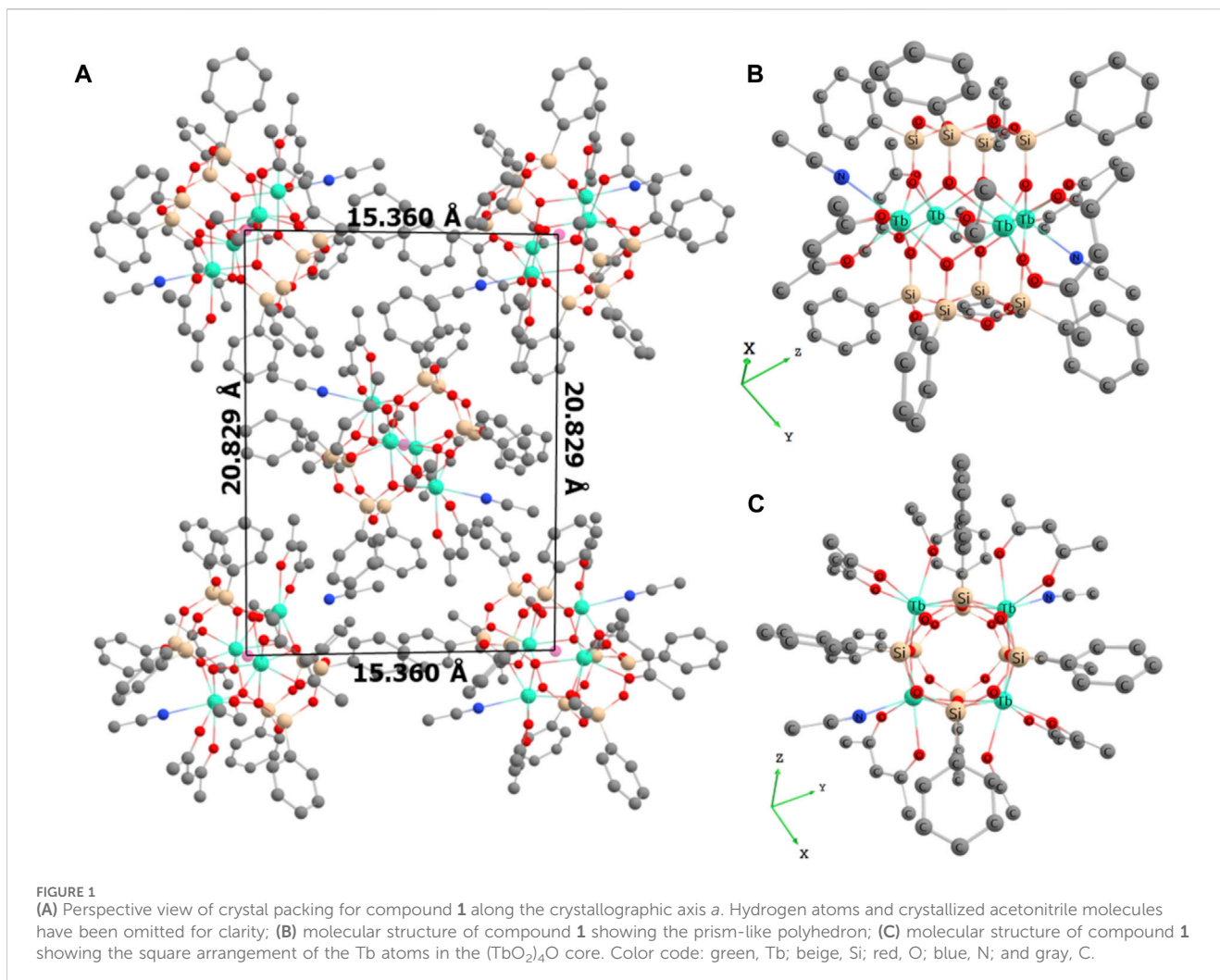
The molecular structure of the neutral tetranuclear lanthanide-based cages of compound **1** may be described as a prism-like polyhedron in the form of a New Year paper lantern. It is formed by a $(\text{TbO}_2)_4$ core wedged between two tetraphenylcyclotetrasiloxanolate moieties ([Figure 1B](#), [C](#) for compound **1**).

For compound **2**, the prism-like polyhedron is formed by a $(\text{Tb}_{1-x}\text{Eu}_x\text{O}_2)_4$ core, where $x = 0.25$, with statistically distributed Tb/Eu ions linked through oxygen atoms, forming a distorted square ([Supplementary Figure S1](#), ESI). In both compounds, there are two slightly different seven-coordinated Tb (for compound **1**) or Tb/Eu sites (for compound **2**), which adopt a one-capped trigonal prism geometry. Each Ln^{3+} ion is coordinated by four bridging oxygens, two oxygens from terminal acetylacetonate, and one ethanol or acetonitrile molecule. The Tb (or Tb/Eu)–O distances involving bridging oxygens are in the range 2.3121(1)–2.3471(1) Å for compound **1** and 2.3013(2)–2.3789(2) Å for compound **2**, while those involving terminal acetylacetonate and ethanol molecules are larger and situated in the range 2.2884(1)–2.3966(1) Å for compound **1** and 2.2822(6)–2.4401(6) Å for compound **2**. The Tb (or Tb/Eu)–N distances involving terminal acetonitrile are 2.5358 (2) Å for compound **1** and in the range 2.4564–2.5691 Å for compound **2**. The O–Ln–O angles in the square are in the range 70.322(3)–81.654(3)° for compounds **1** and **2**. Compound **3** presents crystal structures similar to those of compound **1** ([Supplementary Figure S2](#), ESI). The main distances and angles are given in ESI ([Supplementary Table S2](#)). The atomic Tb/Eu ratio in compound **2** determined by SEM-EDX analysis is equal to 3/1, as expected.

3.2 Magnetic properties

The magnetic measurements were determined for all compounds using a SQUID MPMS-XL magnetometer working between 1.8 and 300 K and up to 7 T.

The temperature dependence of the magnetic susceptibility performed in the direct current (dc) mode has been performed under an applied magnetic field of 1,000 Oe. The room temperature χT values of 48.40 and 31.30 $\text{cm}^3\cdot\text{K}\cdot\text{mol}^{-1}$ for compounds **1** and **2**, respectively, are coherent with the theoretical values of 47.28 and 35.46 $\text{cm}^3\cdot\text{K}\cdot\text{mol}^{-1}$ expected for four (compound **1**) and three Tb^{3+} ions (compound **2**), using the free-ion approximation (7F_6 , $S = 3$, $L = 3$, $g = 3/2$, $\chi T =$



11.82 cm³·K·mol⁻¹) (Long et al., 2011). Upon cooling, the compounds exhibit a typical decrease in χT caused by the thermal depopulation of the Stark sublevels and/or the presence of antiferromagnetic interactions between the Tb³⁺ centers (Figure 2A). The field dependence of magnetization performed at 1.8 K shows a rapid linear increase in the magnetization with the field for both compounds (Figure 2B). The curves do not reach the saturation and magnetization values of 22.9 and 14.95 $N\beta$ under 7T for compounds **1** and **2**, respectively, indicating the presence of significant magnetic anisotropy. This behavior is perfectly coherent with the previously published cage-like compounds containing Tb³⁺ ions. Note that no slow relaxation of the magnetization has been observed by investigation of the dynamic magnetic behaviors of these compounds by alternating current (ac) magnetic measurements.

The magnetic behavior of Gd³⁺-based silsesquioxane **3** is coherent with the presence of four isotropic Gd³⁺ ions. The room temperature χT value of 34.4 cm³·K·mol⁻¹ is in agreement with the expected value (31.52 cm³·K·mol⁻¹) calculated for four Gd³⁺ ions in a free-ion approximation (⁸S_{7/2}, *g* = 2) (Long et al., 2011). As the temperature decreases, the χT vs. *T* curve almost remains constant up to 20 K and then sharply declines at low temperatures, indicating the presence of

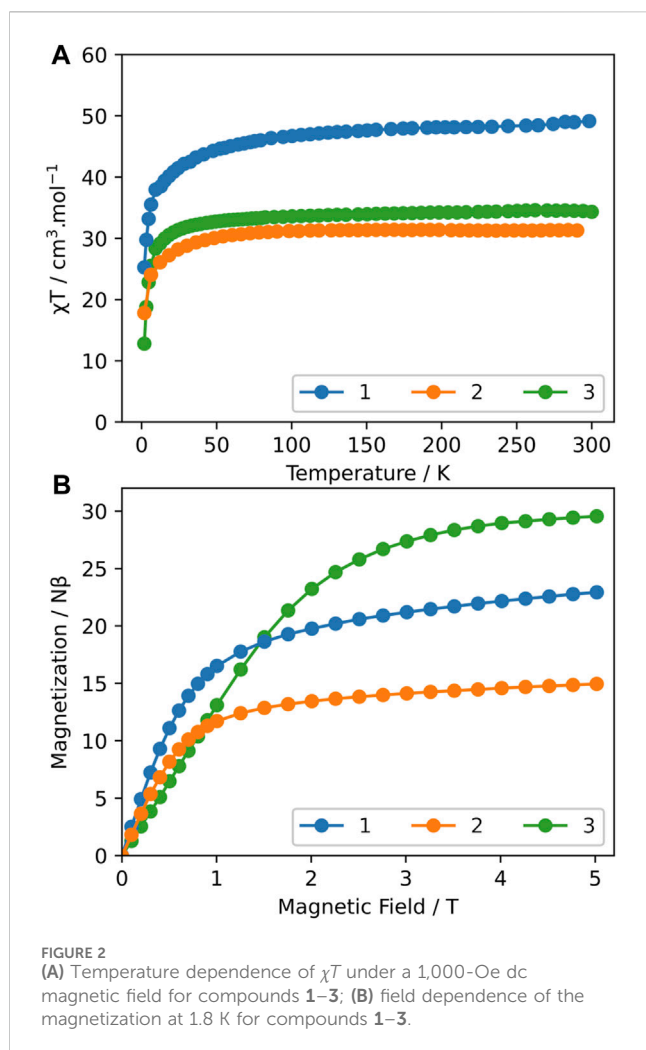
weak antiferromagnetic interactions between adjacent Gd³⁺ ions (Figure 2A). The *M* vs. *H* curve performed at 1.8 K is coherent with the presence of four Gd³⁺ ions (28 $N\beta$) (Figure 2B).

3.3 Experimental and theoretical photoluminescence studies

The excitation and emission spectra of all compounds were investigated in the solid state at different temperatures ranging from 11 to 378 K.

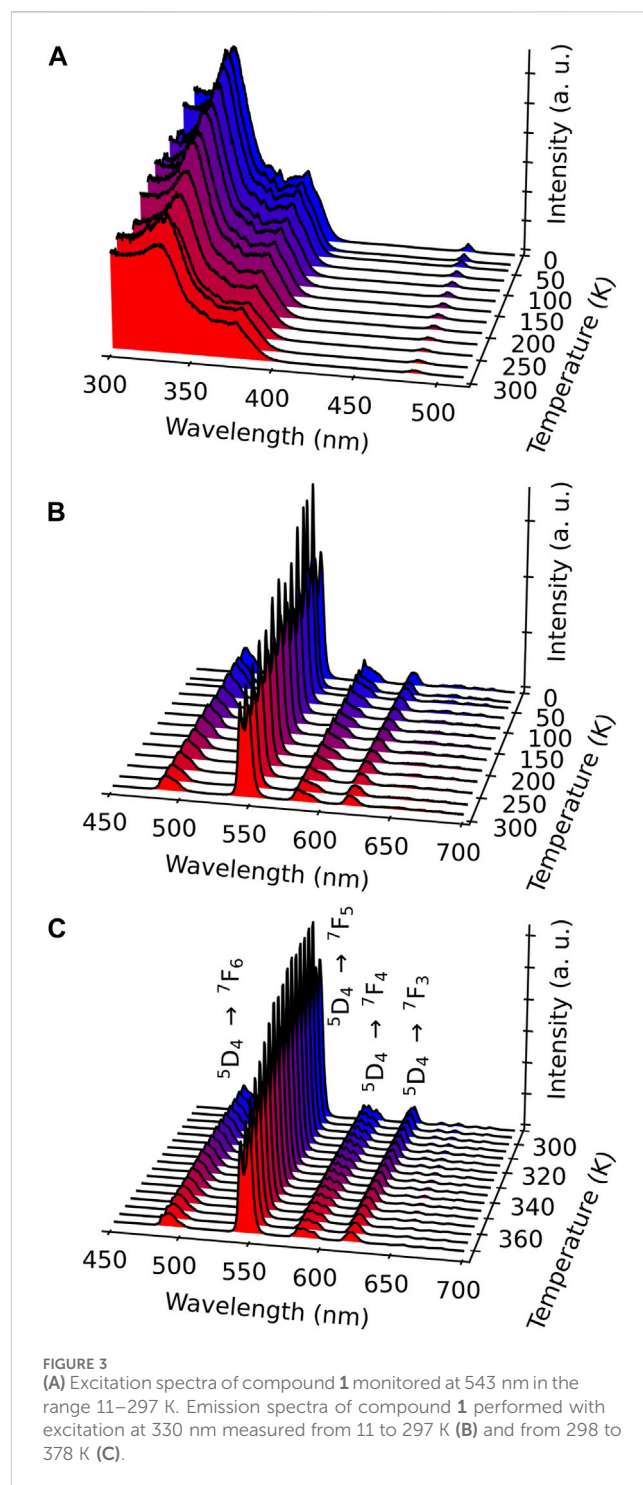
3.3.1 Gd³⁺ compound **3**

The photoluminescence of Gd³⁺-containing compound **3** has been used to assess the energies of the triplet states located on the terminal *acac* ligand since Gd³⁺ has a high energy-accepting electronic level, which prevents any population through the energy transfer from the electronic level of the antenna ligand. Supplementary Figure S3, ESI, shows the emission spectrum of compound **3** obtained upon excitation at 246 nm at 77 K. The energy of the triplet state is 25,316 cm⁻¹ (corresponding to an emission peak at 395 nm).

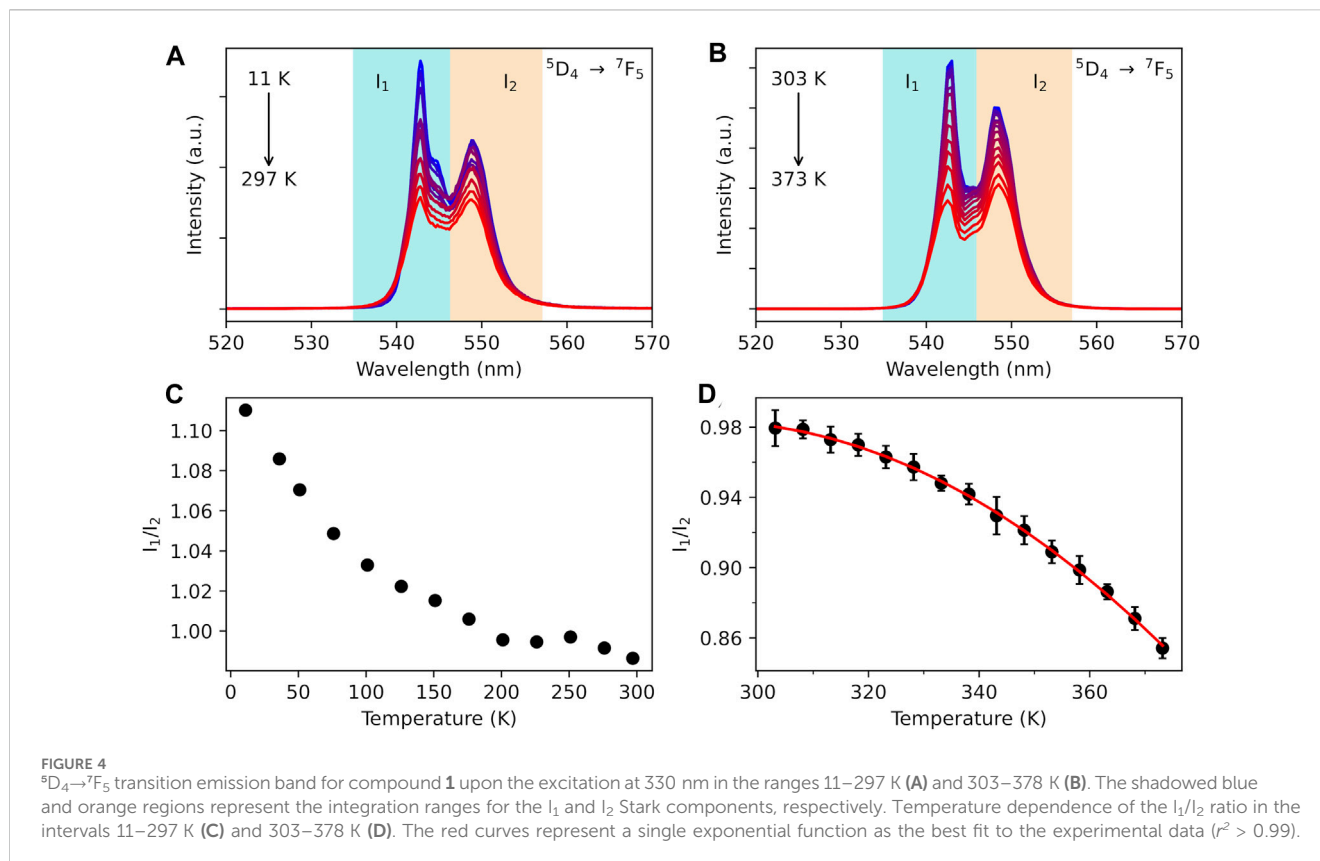


3.3.2 Tb³⁺ compound 1

The excitation spectra of Tb³⁺-containing compound **1** monitored within the main ⁵D₄→⁷F₅ transition (543 nm) in the range 11–300 K exhibit large broadband, with a main component at *ca.* 330 nm attributed to the *acac* ligand excited state (Figure 3A). A series of low-intensity narrow lines attributed to transitions between ⁷F₆ and the ⁵G₅, ⁵G₆, and ⁵D₃ excited states indicates that Tb³⁺ is mainly populated through antenna-assisted sensitization rather than by a direct excitation into the intra-4f⁸ lines. The emission spectra of compound **1** recorded under excitation at 330 nm in the 11–297-K and 298–378-K intervals (Figures 3B,C) exhibit the classical Tb³⁺ ⁵D₄→⁷F_{6,0} characteristic emission lines. The profile of the emission spectra is similar under direct 4f⁸ excitation at 485 nm (Supplementary Figures S4A, B, ESI). The most intense emission, centered at 543 nm, corresponds to the ⁵D₄→⁷F₅ transition, displaying a gradual decrease with increasing temperature, as shown in Figure 4 and Supplementary Figures S4C, S5 (ESI). The emission decay curve of compound **1** was monitored at room temperature within ⁵D₄→⁷F₅. The curve is well-reproduced by a single exponential function, yielding a ⁵D₄ lifetime of 0.851 ± 0.002 ms, which is a rather typical value for Tb³⁺ complexes (Supplementary Figure S6). The presence of two maxima in the ⁵D₄→⁷F₅ transition, *I*₁ and *I*₂ in Figure 4, is associated with two



distinct Stark components. Although the maximum number of ⁵D₄ and ⁷F₅ Stark levels can lead to 99 components in the ⁵D₄→⁷F₅ transition, once the majority is degenerate, only a few can be observed (Figure 4). A question can be raised concerning whether some of these transitions between Stark levels could be attributed to vibronic transitions (or sidebands). This can be answered with the emission spectrum recorded at 11 K (Figure 5A), where vibrational modes that could couple in this spectral region can be suppressed. As the emission intensity is directly proportional to the population of the emitting level, the



model suggests that emission I_1 originates from a Stark component ($|1\rangle$ in Figure 5B) associated with the lower Stark level of 5D_4 . In contrast, emission I_2 comprises the emission from a Stark level with higher energy ($|2\rangle$ in Figure 5B). It is important to note that the high-energy emission is not always attributed to a Stark level with higher energy as the energy of the transition also depends on the energy of the ending level (7F_5), as shown in Figure 5B.

The model assumes that the high-energy emission stems from a lower-energy Stark component of 5D_4 . This assumption is relevant because, at 11 K, there would be no thermal population arising from $|1\rangle$ to $|2\rangle$, and the emission I_2 should vanish at low-temperature ranges because $W_{2 \rightarrow 1} \gg W_{1 \rightarrow 2}$ (Figure 5C), where $W_{2 \rightarrow 1}$ and $W_{1 \rightarrow 2}$ are the multiphonon decay rate (creation of phonons) and absorption (annihilation of phonons) rates, respectively, between $|1\rangle$ and $|2\rangle$ Stark components of the 5D_4 level. The decay rate $W_{2 \rightarrow 1}$ was calculated from the energy gap law (Moos, 1970; Reisfeld et al., 1977; Riseberg et al., 1977; Malkin et al., 2005) in the Miyakawa–Dexter approach (Supplementary Eqs S1,S2) (Miyakawa and Dexter, 1970). The intramolecular energy transfer (IET) rates from T_1 to 5D_4 levels were calculated using Supplementary Eqs S5–S7 (Carneiro Neto et al., 2019) (details given in ESI) using the JOYSpectra web platform (Moura Jr. et al., 2021b).

Based on the obtained IET and multiphonon rates (Figure 5C; Supplementary Table S3), together with the energy level diagram shown in Figures 5A,B, a three-level rate equation model can be considered as follows:

$$\frac{d\eta_1(t)}{dt} = W_{2 \rightarrow 1}\eta_2(t) - \left(W_{1 \rightarrow 2} + \frac{1}{\tau}\right)\eta_1(t) \quad (1)$$

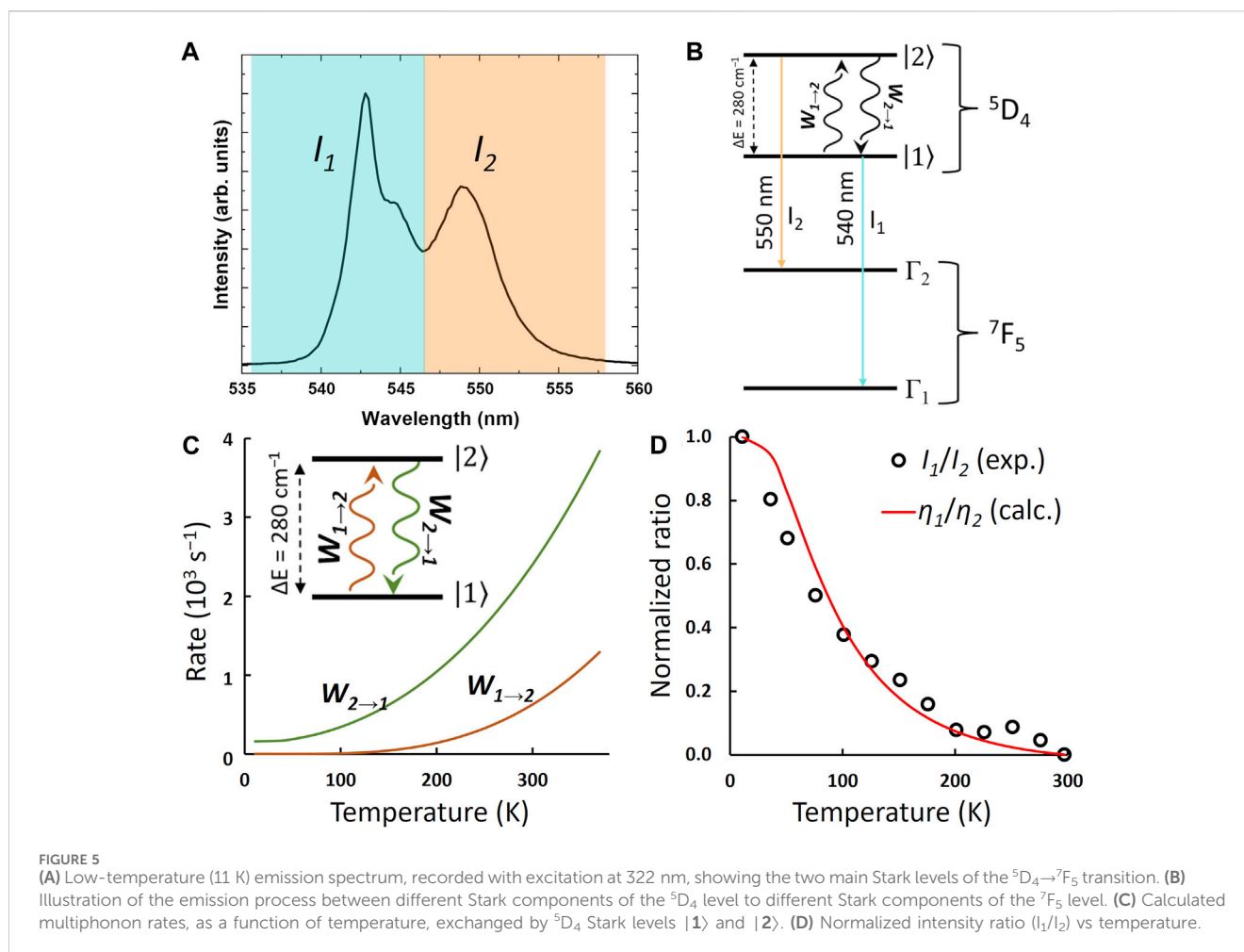
$$\frac{d\eta_2(t)}{dt} = W_{1 \rightarrow 2}\eta_1(t) + \phi\eta_3(t) - \left(W_{2 \rightarrow 1} + \frac{1}{\tau}\right)\eta_2(t) \quad (2)$$

$$\frac{d\eta_3(t)}{dt} = \frac{1}{\tau}[\eta_1(t) + \eta_2(t)] - \phi\eta_3(t) \quad (3)$$

where η_1 , η_2 , and η_3 are the populations of $|1\rangle$, $|2\rangle$, and 7F_5 , respectively, with initial conditions (when $t = 0$) of $\eta_1(0) = \eta_2(0) = 0$ and $\eta_3(0) = 1$. $\tau = 0.851$ ms is the measured decay lifetime of the 5D_4 level, and ϕ is the feeding rate of the emitting level 5D_4 that comes mainly from the energy transfer rates involving the 7F_6 and 7F_5 levels as the starting level (e.g., IET rates from ligand states to $Tb^{3+} {}^7F_6 \rightarrow {}^5D_4$ and ${}^7F_5 \rightarrow {}^5D_4$) (Kasprzycka et al., 2020; Carneiro Neto et al., 2022).

One premise of the present model is that the ϕ feeding rate is attributed to the direct energy transfer from the T_1 state to the 5D_4 level, following the pathways $[T_1 \rightarrow S_0] \rightarrow Tb^{3+} [{}^7F_6 \rightarrow {}^5D_4]$ and $[T_1 \rightarrow S_0] \rightarrow Tb^{3+} [{}^7F_5 \rightarrow {}^5D_4]$ (Supplementary Table S3). It is noteworthy that the last pathway dominates the direct energy transfer process with a rate of 1.9×10^6 s $^{-1}$, and the exchange mechanism (Supplementary Eq. S7) has the most significant contribution (Supplementary Table S3).

Although the energy transfer from the S_1 state has been a recent topic of debate in the literature (Alaoui, 1995; Rodríguez-Cortinas et al., 2002; Yang et al., 2004; Kasprzycka et al., 2017; Moura Jr. et al., 2021a; Aquino LE do et al., 2021; Manzur et al., 2023), as certain levels of Tb^{3+} may serve as better acceptors due to the high values of matrix elements involved in the IET process (e.g., ${}^7F_6 \rightarrow {}^5G_6$ and ${}^7F_5 \rightarrow {}^5G_6$) (Moura Jr. et al., 2021a), the population in the upper levels



essentially decays not as quickly to the $5D_4$ level compared to the rising of the population from the $7F_6$ and $7F_5$ to the $5D_4$ level in the direct energy transfer process. Thus, this premise can be justified by the subsequent multiphonon decay between adjacent levels of Tb^{3+} , forming a ladder-like decay process. These decays are generally slower than direct energy transfer, and consequently, decay steps like $5G_6 \rightarrow 5D_3 \rightarrow 5D_4$ can be neglected in the present model.

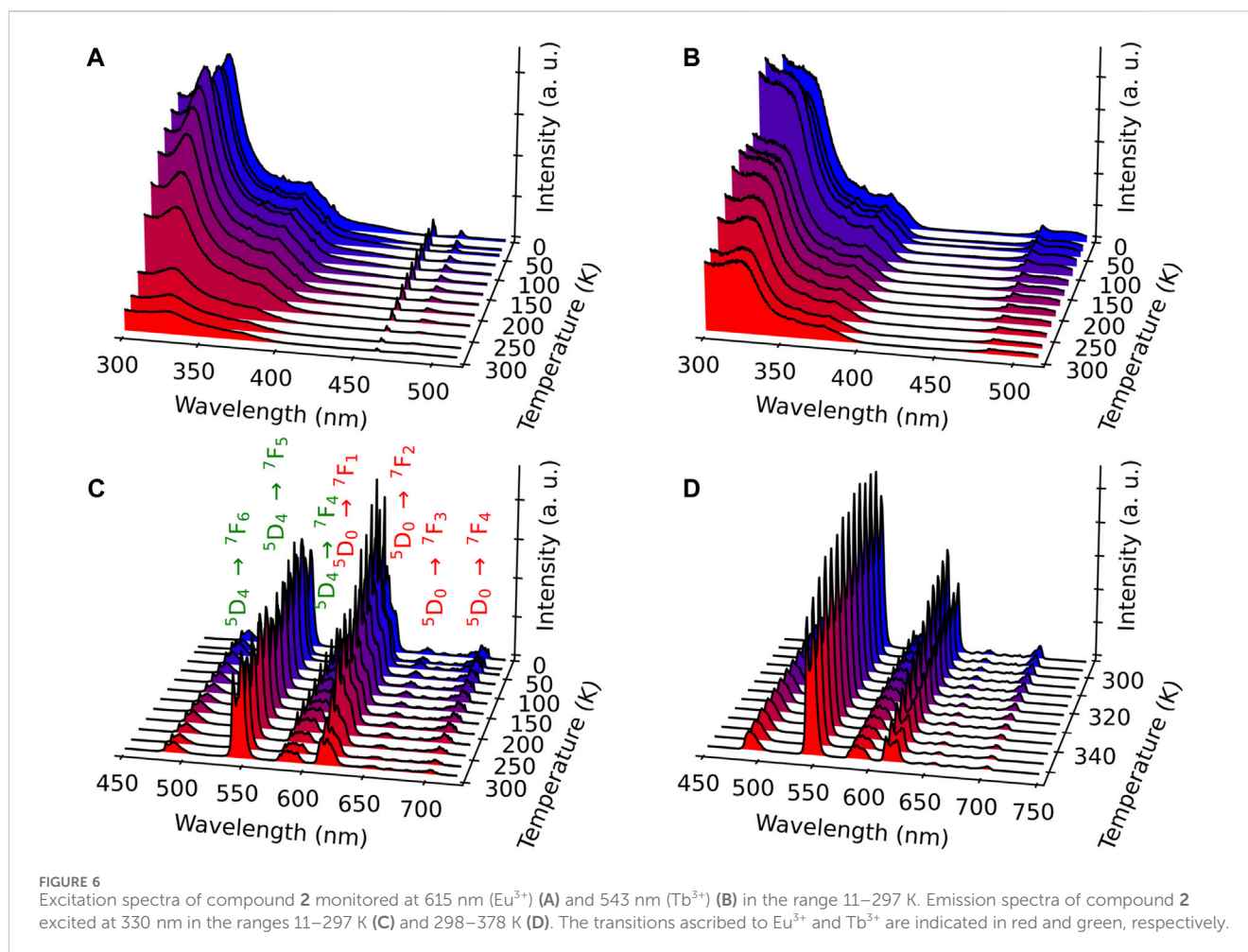
For comparison, the decay from $5D_3 \rightarrow 5D_4$ involves a large energy gap of $\Delta(5D_3 \rightarrow 5D_4) \approx 5,792 \text{ cm}^{-1}$ (Carnall et al., 1978), leading to a decay rate of $W_{mp} = 7.4 \times 10^3 \text{ s}^{-1}$ if two optical phonons with $\hbar\omega = 2,896 \text{ cm}^{-1}$ each are considered to bridge the $\Delta(5D_3 \rightarrow 5D_4)$ gap. This calculation is based on the application of Supplementary Eqs S1, S2 within the energy gap law framework. If a three-phonon process is required to bridge the gap, the multiphonon rate will be even lower ($W_{mp} \sim 60 \text{ s}^{-1}$), as expected when the number of phonons is increased. This underscores that the direct IET rates from the T_1 state are more than two orders of magnitude higher (see Supplementary Table S3) than the multiphonon decay in the $5D_4$ sensitization process.

The rate equation model (Supplementary Eqs S1–S3) was numerically propagated using the Radau method, a numerical approach belonging to the class of fully implicit Runge–Kutta methods (Hairer et al., 2015), over a time span of 0–10 ms with a step size of 10 ns. This implies that 1,000,000 points were

calculated for each temperature, ranging from 11 to 297 K in steps of 2 K.

As the intensity is directly proportional to the population of the emitting level, the experimental intensity ratio (I_1/I_2 in Figure 4) and the calculated population ratio (η_1/η_2) in the steady-state regime can be compared. Figure 5D illustrates this comparison, and it can be concluded that the calculated trend is similar to the experimental trend. This observation suggests that the Stark components of the $5D_4$ are governed by an equilibrium between non-radiative decay and rising among these components ($|1\rangle$ and $|2\rangle$), driven by a Boltzmann distribution between $W_{2\rightarrow 1}$ and $W_{1\rightarrow 2}$.

Suta and Meijerink (2020) reported that there is potential temperature dependence in the use of crystal field splitting (Stark levels) for trivalent lanthanides at low temperatures. However, at higher temperatures, where the product $k_B T$ is significantly greater than the crystal splitting energy, a thermodynamic equilibrium among Stark levels could be established, allowing for their treatment as an effectively thermally averaged single level with an average radiative decay rate. In our model, this implies that the non-radiative decays and absorptions between two Stark levels are approximately equal, rendering the model inapplicable. In other words, Boltzmann statistics between Stark levels become ineffective at higher temperatures, resulting in a shift in the trend for temperatures exceeding 250 K, as shown in Supplementary Figure



S5A (ESI), and consistent with the behavior shown in Supplementary Figure S5B (ESI).

3.3.3 Mixed Eu³⁺/Tb³⁺ compound 2

To provide a self-calibrated ratiometric luminescent thermometer, the Eu³⁺ ion was introduced in the structure to obtain compound 2, as previously demonstrated in different MOF materials and Ln³⁺-based complexes (Brites et al., 2019). The excitation spectra at different temperatures were recorded by monitoring the main emissions of both Eu³⁺ at 615 nm (⁵D₀→⁷F₂) and Tb³⁺ at 543 nm (⁵D₄→⁷F₅) (Figures 6A,B). The spectra are relatively similar and, as in the case of compound 1, present main broadband (at 330 nm) attributed to the *acac* ligand excited states, confirming the excitation through antenna sensitization. Low-intensity intra-4f transitions of both Ln³⁺ ions can also be visible in the spectra, e.g., ⁷F_{0,1}→⁵D₂ (Figure 6A) and ⁷F₆→⁵D₄ (Figures 6A,B). The observation of this latter Tb³⁺ line when monitoring Eu³⁺ emission at 615 nm points out the occurrence of Tb³⁺-to-Eu³⁺ energy transfer.

The emission spectra were measured upon excitation at 330 nm, which is operational for both Ln³⁺ ions, in the ranges 11–297 K (Figure 6C) and 298–378 K (Figure 6D). Compared with the emission spectra of compound 1, the Eu³⁺-characteristic transitions from ⁵D₀ to ⁷F_J (J = 0–4) appear besides the Tb³⁺ transitions. Note that the emission spectra obtained under a

direct excitation at 484 nm (Tb³⁺ ⁷F₆→⁵D₄ transition) show, besides the main Tb³⁺ transition ⁵D₄→⁷F₅ (indicated in green), a series of the Eu³⁺-related transitions ⁵D₀→⁷F_{1,2,3,4} (indicated in red, Supplementary Figure S7, ESI). This fact points out the presence of the Tb³⁺-to-Eu³⁺ energy transfer, as already inferred from the excitation spectra shown in Figure 6B. This is not surprising considering that the shortest Ln³⁺-Ln³⁺ distance in compound 2 is equal to 3.728 Å. As expected, the emission spectra performed with direct excitation in the Eu³⁺-related band at 464 nm display only the Eu³⁺ transitions (Supplementary Figure S8, ESI).

To estimate the energy transfer rates, in addition to the calculations of pairwise interactions (Malta, 2008; Carneiro Neto et al., 2020), the distribution of donor–acceptor distances, where Tb³⁺ is the donor and Eu³⁺ is the acceptor, was calculated from the crystallographic structure using a custom program written in C. The simulations of the Tb³⁺/Eu³⁺ ratio (3:1) in the structure of an expanded 20 × 20 × 20 crystal, consisting of 64,000 Ln³⁺ sites, were conducted. The sites could be occupied by either Tb³⁺ or Eu³⁺ ions. The program performed 100 simulations while maintaining the 3:1 ratio to provide statistically reliable donor–acceptor distance results. Thus, the occurrence of the formation of a Tb–Eu pair with a given distance is given by (Trannoy et al., 2021)

$$O_i = \frac{\mathcal{N}_i}{s \cdot x} \quad (4)$$

where \mathcal{N}_i is the counting of a donor–acceptor pair with distance $R(i)$, $s = 64,000$ is the number of total host sites (i.e., Ln^{3+} sites) available for Eu^{3+} and Tb^{3+} substitution, and x is the fraction of Eu^{3+} ($x = 0.25$ for forward energy transfer) or Tb^{3+} ($x = 0.75$ for backward energy transfer).

Figure 1A and Supplementary Figure S1, ESI, show that the shortest distance between two $\{\text{Ln}_4\}$ clusters of Ln^{3+} is in the order of 15 Å. This results in a weak interaction concerning Tb–Eu energy transfer between different $\{\text{Ln}_4\}$ clusters. Thus, the Tb–Eu interaction is restricted to intra-cluster energy transfer, which can lead to highly effective energy transfer rates, as discussed in the literature (Wang et al., 2014; Calado et al., 2023; Gálico et al., 2023; Pelluau et al., 2023).

Using the calculated Tb–Eu pairwise energy transfer rates (see Supplementary Table S4 and the theoretical section in the ESI for further details) and the O_i coefficients (Supplementary Table S5; Eq. 4) obtained from doping simulations of Tb^{3+} and Eu^{3+} , the average (or effective) energy transfer rates from Tb-to-Eu can be estimated as (Trannoy et al., 2021)

$$\langle W \rangle = \sum_{i=1}^4 \langle W \rangle_i = (1-x)x \sum_{i=1}^4 O_i \cdot W_i \quad (5)$$

where $x = 0.25$ is the fraction of Eu^{3+} in the compound and W_i represents the pairwise Tb–Eu energy transfer for the i th distance (Supplementary Table S5).

Supplementary Figure S9 illustrates the temperature behavior of W_i and $\langle W \rangle$. Although the temperature increase provides high Eu^{3+} sensitization, the emission of Eu^{3+} undergoes quenching (Figures 6C,D), probably due to high-energy phonons that may couple with the $^5\text{D}_0$ level. Thus, although intra-cluster Tb^{3+} -to- Eu^{3+} energy transfer can provide high rates in contrast to non-clustering systems (Carneiro Neto et al., 2020; Trannoy et al., 2021), there are other factors in the chemical environment around Ln^{3+} that may act as a quenching channel, in this case, selectively affecting the Eu^{3+} ion, while the decrease in the intensity of the Tb^{3+} emissions may be related to the increase in the Tb^{3+} -to- Eu^{3+} rates with temperature.

To demonstrate the possibility of using compound 2 as a self-referenced luminescent thermometer, temperature dependence of the normalized integrated intensity area related with the two main transitions $\text{Tb}^{3+} \ ^5\text{D}_4 \rightarrow ^7\text{F}_5$ (in green) and $\text{Eu}^{3+} \ ^5\text{D}_0 \rightarrow ^7\text{F}_2$ (in red) was extracted for both emission spectra obtained upon excitations at 330 nm (antenna) and 484 nm (intra- $4f^8$). The temperature-dependent variation in the corresponding thermometric parameter ($I_{5\text{D}_4 \rightarrow 7\text{F}_5} / I_{5\text{D}_0 \rightarrow 7\text{F}_2}$, LIR) in the ranges 11–297 K (Figure 7A) and 298–378 K (Figure 7B) shows exponential correlations, which can be used for temperature measurements. The relative thermal sensitivity (S_r) is the main parameter, allowing the comparison of the performance among different types of thermometers (Bednarkiewicz et al., 2020). The S_r value represents the variation in the experimental thermometric parameter (LIR in the present case) per degree of temperature, which is expressed as

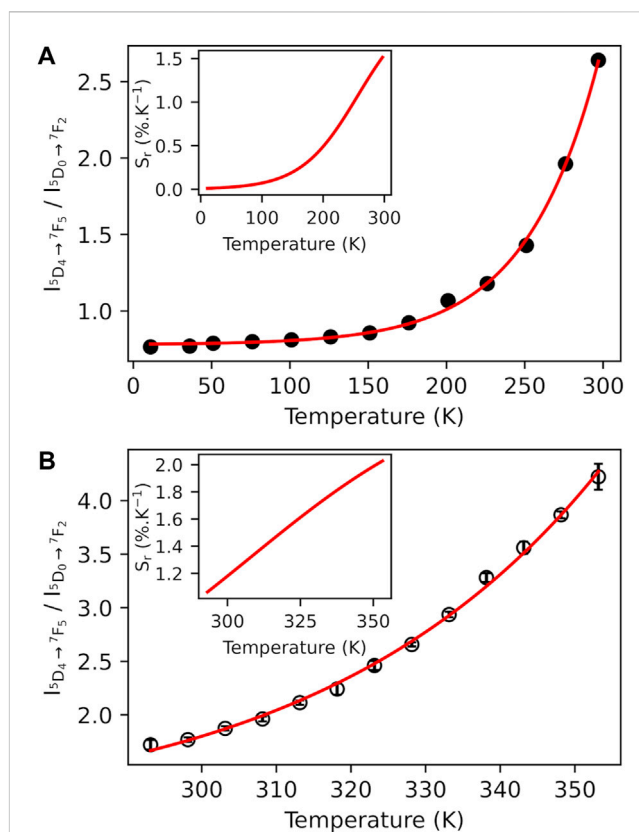


FIGURE 7 Temperature dependence of the normalized luminescence intensity ($I_{5\text{D}_4 \rightarrow 7\text{F}_5} / I_{5\text{D}_0 \rightarrow 7\text{F}_2}$) performed for the emission spectra of compound 2 under the excitation at 330 nm in the ranges 11–297 K (A) and 298–378 K (B) with several experimental cycles (circles) and the associated fit (red curve) with a single exponential function (full line) ($r^2 > 0.99$). Inset: S_r , temperature dependence.

$$S_r(T) = \frac{1}{\text{LIR}(T)} \left| \frac{\partial \text{LIR}(T)}{\partial T} \right| \quad (6)$$

The temperature dependences of S_r are shown in the insets of Figures 7A,B. The maximum S_r value is equal to $1.5\% \cdot \text{K}^{-1}$ at 297 K, for 11–297 K, and $2.0\% \cdot \text{K}^{-1}$ at 373 K, for 298–378 K. Both values are close to a frequently considered high relative thermal sensitivity ($\sim 1\% \cdot \text{K}^{-1}$) (Brites et al., 2019) and are close to the best S_r values reported for mixed $\text{Eu}^{3+}/\text{Tb}^{3+}$ compounds (Trannoy et al., 2021). Temperature uncertainty (or thermal resolution, δT) is the smallest temperature change that can be detected (Brites et al., 2016). This value is related to S_r as follows:

$$\delta T = \frac{1}{S_r(T)} \left| \frac{\delta \text{LIR}(T)}{\text{LIR}(T)} \right| \quad (7)$$

where $\delta \text{LIR}(T)$ is the standard deviation in the $\text{LIR}(T)$ obtained upon several temperature cycles. According to this, the minimal thermal resolution is 0.2 K. Note that the use of emission spectra upon excitation at 484 nm for thermometry is also possible. Supplementary Figures S10A, B, ESI show the corresponding temperature dependences of LIR and the maximal value of S_r of $1.3\% \cdot \text{K}^{-1}$ at 297 K. Therefore, the

temperature sensor **2** proposed here works reliably in the operating range 11–378 K.

The emission decay curves of compound **2** were monitored at room temperature upon excitation at 330 nm within the $^5D_4 \rightarrow ^7F_6$ (Tb^{3+}) and $^5D_0 \rightarrow ^7F_4$ (Eu^{3+}) transitions (Supplementary Figure S11, ESI). The curves are well-reproduced by double-exponential functions as the best fits to the experimental data ($r^2 > 0.99$), yielding lifetimes of 0.126 ± 0.002 and 0.668 ± 0.002 ms for the former and 0.110 ± 0.002 and 0.406 ± 0.002 ms for the latter transitions. The occurrence of two lifetimes is under investigation and will be addressed later.

4 Conclusion

In summary, here, we reported three new luminescent cage-like silsesquioxanes containing a tetranuclear Tb^{3+} , Tb^{3+}/Eu^{3+} , or Gd^{3+} core, where each Ln^{3+} ion is coordinated by an antenna acetylacetonate ligand. The crystal structures indicate that the introduction of chelating acetylacetonate changes the coordination environment of the Ln^{3+} ions conducting to seven-coordination geometry close to the one-capped trigonal prism.

Lanthanide-based silsesquioxanes **1** and **2** present solid-state characteristic Tb^{3+} and Tb^{3+}/Eu^{3+} -related emissions between 11 and 373 K sensitized by acetylacetonate antenna upon excitation in the UV region, while the direct excitation in the visible domain is also possible.

Theoretical calculations were conducted to elucidate the primary characteristics of the thermal behavior between the Stark levels of the 5D_4 level in compound **1**. The results demonstrated good agreement between experiment and theory, enabling the extraction of the main effect, which is the balance between multiphonon decays and absorptions between these two Stark levels as a function of temperature.

For compound **2**, where intra-cluster energy transfer can be highly efficient and even surpass the ligand-to- Ln^{3+} transfer, simulations were performed to obtain the average Tb^{3+} -to- Eu^{3+} energy transfer rates within the $\{Ln_4\}$ cluster structure. The analysis revealed that the average energy transfer increases with temperature, consistent with the low quenching observed for Tb^{3+} emissions. Conversely, the abrupt quenching of Eu^{3+} emissions with increasing temperature suggests a strong electron-phonon coupling for this ion.

Mixed Tb^{3+}/Eu^{3+} (Tb/Eu ration 3/1) compound **2** exhibits a tunable thermosensitive Tb^{3+} -to- Eu^{3+} energy transfer driven by Tb^{3+} and Eu^{3+} emissions. The corresponding temperature dependence allows the verification of the use of this compound for a ratiometric self-reference luminescent thermometer. It was realized by using a fluorescence intensity ratio between the two main components of the spectra ($Tb^{3+} \ ^5D_4 \rightarrow ^7F_5$ and $Eu^{3+} \ ^5D_0 \rightarrow ^7F_2$ transitions) in the range 11–373 K, demonstrating the maximum relative thermal sensitivity referred above 2.0 % K^{-1} at 373 K.

Data availability statement

The original contributions presented in the study are included in the article/Supplementary Material; further inquiries can be directed to the corresponding authors.

Author contributions

GF: data curation, investigation, methodology, supervision, validation, and writing–original draft. AK: data curation, formal analysis, investigation, methodology, and writing–original draft. SS: data curation, formal analysis, investigation, supervision, validation, and writing–original draft. VK: data curation, formal analysis, investigation, software, and writing–original draft. MH-R: data curation, formal analysis, investigation, and writing–original draft. ES: supervision, writing–original draft, and funding acquisition. TP: writing–original draft, data curation, formal analysis, and investigation. LC: conceptualization, funding acquisition, project administration, resources, supervision, validation, writing–original draft, and writing–review and editing. YG: conceptualization, funding acquisition, supervision, validation, writing–original draft, writing–review and editing, and investigation. AC: investigation, validation, writing–original draft, writing–review and editing, data curation, formal analysis, software, and visualization. AB: validation, writing–original draft, writing–review and editing, conceptualization, funding acquisition, methodology, and supervision. JL: conceptualization, methodology, supervision, validation, writing–original draft, writing–review and editing, funding acquisition, project administration, and visualization.

Funding

The author(s) declare that financial support was received for the research, authorship, and/or publication of this article. This work was financially supported by the Russian Science Foundation (project No. 22-13-00250, synthetic and luminescent studies), the University of Montpellier and CNRS, and the project PRC2287 Premium 2019–2021. Elemental analysis data were collected using the equipment of the Center for Molecular Composition Studies of INEOS RAS with support from the Ministry of Science and Higher Education of the Russian Federation. JL acknowledges the Vernadsky program of the Embassy of France in the Russian Federation (2019–2021). This project was developed within the scope of the national program ANR (Project Hotspot), France. MAHR acknowledges the Beatriz Galindo Fellowship (BG22/00061). This work was also developed within the scope of the projects CICECO, Aveiro Institute of Materials, UIDB/50011/2020, UIDP/50011/2020, and LA/P/0006/2020 financed by Portuguese funds through the FCT/MCTES (PIDDAC).

Acknowledgments

The authors acknowledge the Platform of Analysis and Characterization (PAC) of ICGM for providing magnetic and X-ray diffraction measurements.

Conflict of interest

The authors declare that the research was conducted in the absence of any commercial or financial relationships that could be construed as a potential conflict of interest.

The author(s) declared that they were an editorial board member of Frontiers, at the time of submission. This had no impact on the peer review process and the final decision.

Publisher's note

All claims expressed in this article are solely those of the authors and do not necessarily represent those of their affiliated organizations, or those of the publisher, the editors, and the

reviewers. Any product that may be evaluated in this article, or claim that may be made by its manufacturer, is not guaranteed or endorsed by the publisher.

Supplementary material

The Supplementary Material for this article can be found online at: <https://www.frontiersin.org/articles/10.3389/fchem.2024.1379587/full#supplementary-material>

References

- Alaoui, I. M. (1995). Nonparticipation of the ligand's first triplet state in intramolecular energy transfer in Eu^{3+} and Tb^{3+} ruthmann's purple complexes. *J. Phys. Chem.* 99 (35), 13280–13282. doi:10.1021/j100035a036
- Allison, S. W. (2019). A brief history of phosphor thermometry. *Meas. Sci. Technol.* 30 (7), 072001. doi:10.1088/1361-6501/ab1d02
- Annand, J., Aspinall, H. C., and Steiner, A. (1999). Novel heterometallic lanthanide silsesquioxane. *Inorg. Chem.* 38 (17), 3941–3943. doi:10.1021/ic990208p
- Annand, J., and Aspinall, H. C. (2000). Lanthanide silsesquioxanes: monomeric and functionalised complexes. *J. Chem. Soc. Dalton Trans.* 0 (12), 1867–1871. doi:10.1039/b000659j
- Aquino Le do, N., Barbosa, G. A., Ramos, J. de L., Giese S, O. K., Santana, F. S., Hughes, D. L., et al. (2021). Seven-coordinate Tb^{3+} complexes with 90% quantum yields: high-performance examples of combined singlet- and triplet-to- Tb^{3+} energy-transfer pathways. *Inorg. Chem.* 60 (2), 892–907. doi:10.1021/acs.inorgchem.0c03020
- Arnold, P. L., Blake, A. J., Hall, S. N., Ward, B. D., and Wilson, C. (2001). A functional model for lanthanide doped silicate materials: synthesis of an apically substituted samarium silsesquioxane complex. *J. Chem. Soc. Dalton Trans.* 0 (4), 488–491. doi:10.1039/b009123p
- Aulsebrook, M. L., Graham, B., Grace, M. R., and Tuck, K. L. (2018). Lanthanide complexes for luminescence-based sensing of low molecular weight analytes. *Coord. Chem. Rev.* 375, 191–220. doi:10.1016/j.ccr.2017.11.018
- Bednarkiewicz, A., Marciniak, L., Carlos, L. D., and Jaque, D. (2020). Standardizing luminescence nanothermometry for biomedical applications. *Nanoscale.* 12 (27), 14405–14421. doi:10.1039/d0nr03568h
- Bernot, K., Daigebonne, C., Calvez, G., Suffren, Y., and Guillou, O. (2021). A journey in lanthanide coordination chemistry: from evaporable dimers to magnetic materials and luminescent devices. *Acc. Chem. Res.* 54 (2), 427–440. doi:10.1021/acs.accounts.0c00684
- Bettinelli, M., Carlos, L., and Liu, X. (2015). Lanthanide-doped upconversion nanoparticles. *Phys. Today.* 68 (9), 38–44. doi:10.1063/pt.3.2913
- Bodman, S. E., and Butler, S. J. (2021). Advances in anion binding and sensing using luminescent lanthanide complexes. *Chem. Sci.* 12 (8), 2716–2734. doi:10.1039/d0sc05419d
- Brites, C. D. S., Balabhadra, S., and Carlos, L. D. (2019). Lanthanide-based thermometers: at the cutting-edge of luminescence thermometry. *Adv. Opt. Mater.* 7 (5), 1801239. doi:10.1002/adom.201801239
- Brites, C. D. S., Lima, P. P., Silva, N. J. O., Millán, A., Amaral, V. S., Palacio, F., et al. (2010). A luminescent molecular thermometer for long-term absolute temperature measurements at the nanoscale. *Adv. Mater.* 22 (40), 4499–4504. doi:10.1002/adma.201001780
- Brites, C. D. S., Lima, P. P., Silva, N. J. O., Millán, A., Amaral, V. S., Palacio, F., et al. (2012). Thermometry at the nanoscale. *Nanoscale* 4 (16), 4799–4829. doi:10.1039/c2nr30663h
- Brites, C. D. S., Marin, R., Suta, M., Carneiro Neto, A. N., Ximendes, E., Jaque, D., et al. (2023). Spotlight on luminescence thermometry: basics, challenges, and cutting-edge applications. *Adv. Mater.* 35, 2302749. doi:10.1002/adma.202302749
- Brites, C. D. S., Millán, A., and Carlos, L. D. (2016). "Chapter 281 - lanthanides in luminescent thermometry," in *Handbook on the physics and chemistry of rare earths*. Editors B. Jean-Claude and K. P. Vitalij (Elsevier), 339–427. doi:10.1016/bs.hpcr.2016.03.005
- Bünzli, J. C. G. (2010). Lanthanide luminescence for biomedical analyses and imaging. *Chem. Rev.* 110 (5), 2729–2755. doi:10.1021/cr900362e
- Bünzli, J. C. G. (2015). On the design of highly luminescent lanthanide complexes. *Coord. Chem. Rev.* 293–294, 19–47. doi:10.1016/j.ccr.2014.10.013
- Bünzli, J. C. G. (2019). Lanthanide photonics: shaping the nanoworld. *TRECHEM.* 1 (8), 751–762. doi:10.1016/j.trechm.2019.05.012
- Bünzli, J. C. G., and Eliseeva, S. V. (2013). Intriguing aspects of lanthanide luminescence. *Chem. Sci.* 4 (5), 1939–1949. doi:10.1039/c3sc22126a
- Calado, C. M. S., Gálico, D. A., and Murugesu, M. (2023). Intra-cluster energy transfer editing in a dual-emitting system to tap into lifetime thermometry. *Chem. Commun.* 59 (92), 13715–13718. doi:10.1039/d3cc03658h
- Carnall, W. T., Crosswhite, H., and Crosswhite, H. M. (1978). "Energy level structure and transition probabilities in the spectra of the trivalent lanthanides in LaF_3 ." Report No.: ANL-78-XX-95. Available at: <https://www.osti.gov/biblio/6417825> (Accessed December 12, 2023).
- Carneiro Neto, A. N., Kasprzycka, E., Souza, A. S., Gawryszewska, P., Suta, M., Carlos, L. D., et al. (2022). On the long decay time of the $^7\text{F}_5$ level of Tb^{3+} . *J. Luminescence.* 248, 118933. doi:10.1016/j.jlumin.2022.118933
- Carneiro Neto, A. N., Moura, R. T., Jr., Shyichuk, A., Paterlini, V., Piccinelli, F., Bettinelli, M., et al. (2020). Theoretical and experimental investigation of the $\text{Tb}^{3+} \rightarrow \text{Eu}^{3+}$ energy transfer mechanisms in cubic $\text{A}_3\text{Tb}_{0.90}\text{Eu}_{0.10}(\text{PO}_4)_3$ (A = Sr, Ba) materials. *J. Phys. Chem. C* 124 (18), 10105–10116. doi:10.1021/acs.jpcc.0c00759
- Carneiro Neto, A. N., Teotonio, E. E. S., de Sá, G. F., Brito, H. F., Legendziewicz, J., Carlos, L. D., et al. (2019). "Chapter 310 - modeling intramolecular energy transfer in lanthanide chelates: a critical review and recent advances," in *Handbook on the physics and chemistry of rare earths*. Editors J. C. G. Bünzli and V. K. Pecharsky (Elsevier), 55–162.
- Choi, S. H., Duzik, A. J., Kim, H. J., Park, Y., Kim, J., Ko, H. U., et al. (2017). Perspective and potential of smart optical materials. *Smart Mater Struct.* a0126 (9), 093001. doi:10.1088/1361-665x/aa7c32
- Costa, I. F., Blois, L., Paolini, T. B., Assunção, I. P., Teotonio, E. E. S., Felinto, MCFC, et al. (2024). Luminescence properties of lanthanide tetrakis complexes as molecular light emitters. *Coord. Chem. Rev.* 502, 215590. doi:10.1016/j.ccr.2023.215590
- Cui, Y., Xu, H., Yue, Y., Guo, Z., Yu, J., Chen, Z., et al. (2012). A luminescent mixed-lanthanide metal-organic framework thermometer. *J. Am. Chem. Soc.* 134 (9), 3979–3982. doi:10.1021/ja2108036
- Davies, G. L., O'Brien, J., and Gun'ko, Y. K. (2017). Rare earth doped silica nanoparticles via thermolysis of a single source metallasilsesquioxane precursor. *Sci. Rep.* 7 (1), 45862. doi:10.1038/srep45862
- de Sá, G. F., Malta, O. L., de Mello Donegá, C., Simas, A. M., Longo, R. L., Santa-Cruz, P. A., et al. (2000). Spectroscopic properties and design of highly luminescent lanthanide coordination complexes. *Coord. Chem. Rev.* 196 (1), 165–195. doi:10.1016/s0010-8545(99)00054-5
- Dramićanin, M. D. (2020). Trends in luminescence thermometry. *J. Appl. Phys.* 128 (4), 040902. doi:10.1063/5.0014825
- Eliseeva, S. V., and Bünzli, J. C. G. (2009). Lanthanide luminescence for functional materials and bio-sciences. *Chem. Soc. Rev.* 39 (1), 189–227. doi:10.1039/b905604c
- Félix, G., Kulakova, A., Sene, S., Charlot, C., Bilyachenko, A. N., Korlyukov, A. A., et al. (2023a). Tetranuclear lanthanide-based silsesquioxanes: towards a combination of germesquioxanes: luminescence and temperature sensing. *Organometallics* 42 (18), 2613–2622. doi:10.1021/acs.organomet.3c00009
- Félix, G., Sene, S., Kulakova, A., Bilyachenko, A. N., Khrustalev, V. N., Shubina, E. S., et al. (2023b). Tetranuclear lanthanide-based silsesquioxanes: towards a combination of a slow relaxation of the magnetization and a luminescent thermometry. *RSC Adv.* 13 (37), 26302–26312. doi:10.1039/d3ra04901a
- Fernandes, M., Freitas, V., Pereira, S., Leones, R., Silva, M. M., Carlos, L. D., et al. (2018). Luminescent electrochromic devices for smart windows of energy-efficient buildings. *Energies.* 11 (12), 3513. doi:10.3390/en1123513

- Ferreira da Rosa, P. P., Kitagawa, Y., and Hasegawa, Y. (2020). Luminescent lanthanide complex with seven-coordination geometry. *Coord. Chem. Rev.* 406, 213153. doi:10.1016/j.ccr.2019.213153
- Gálco, D. A., Calado, C. M. S., and Murugesu, M. (2023). Lanthanide molecular cluster-aggregates as the next generation of optical materials. *Chem. Sci.* 14 (22), 5827–5841. doi:10.1039/d3sc01088k
- Gregório, T., Leão, J. D. M., Barbosa, G. A., Ramos, J. de L., Kumar Giese, O. S., Briganti, M., et al. (2019). Promoting a significant increase in the photoluminescence quantum yield of terbium(III) complexes by ligand modification. *Inorg. Chem.* 58 (18), 12099–12111. doi:10.1021/acs.inorgchem.9b01397
- Hairer, E., and Wanner, G. (2015). “Radau methods,” in *Encyclopedia of applied and computational mathematics*. Editor B. Engquist (Berlin, Heidelberg: Springer), 1213–1216. doi:10.1007/978-3-540-70529-1_139
- Herrmann, W. A., Anwander, R., Dufaud, V., and Scherer, W. (1994). Molecular siloxane complexes of rare earth metals—model systems for silicate-supported catalysts? *Angewandte Chemie Int. Ed. Engl.* 33 (12), 1285–1286. doi:10.1002/anie.199412851
- Jaque, D., and Vetrone, F. (2012). Luminescence nanothermometry. *Nanoscale* 4 (15), 4301–4326. doi:10.1039/c2nr30764b
- Kaczmarek, A. M., Deun, R. V., and Voort, P. V. D. (2019). Nanothermometers based on lanthanide incorporated periodic mesoporous organosilica. *J. Mater. Chem. C* 7 (14), 4222–4229. doi:10.1039/c8tc06353b
- Kasprzycka, E., Carneiro Neto, A. N., Trush, V. A., Jerzykiewicz, L., Amirkanov, V. M., Malta, O. L., et al. (2020). How minor structural changes generate major consequences in photophysical properties of RE coordination compounds; resonance effect, LMCT state. *J. Rare Earths* 38 (5), 552–563. doi:10.1016/j.jre.2020.02.001
- Kasprzycka, E., Trush, V. A., Amirkanov, V. M., Jerzykiewicz, L., Malta, O. L., Legendziewicz, J., et al. (2017). Contribution of energy transfer from the singlet state to the sensitization of Eu^{3+} and Tb^{3+} luminescence by sulfonamidophosphates. *Chem. – A Eur. J.* 23 (6), 1318–1330. doi:10.1002/chem.201603767
- Kulakova, A. N., Bilyachenko, A. N., Levitsky, M. M., Khrustalev, V. N., Shubina, E. S., Félix, G., et al. (2020). New luminescent tetranuclear lanthanide-based silsesquioxane cage-like architectures. *Chem. – A Eur. J.* 26 (70), 16567–16568. doi:10.1002/chem.202004207
- Kulakova, A. N., Nigoghossian, K., Félix, G., Khrustalev, V. N., Shubina, E. S., Long, J., et al. (2021). New magnetic and luminescent Dy(III) and Dy(III)/Y(III) based tetranuclear silsesquioxane cages. *Eur. J. Inorg. Chem.* 2021 (27), 2696–2701. doi:10.1002/ejic.202100308
- Laird, M., Totée, C., Gaveau, P., Silly, G., Lee, A. V. D., Carcel, C., et al. (2021). Functionalised polyhedral oligomeric silsesquioxane with encapsulated fluoride – first observation of fluxional Si...F interactions in POSS. *Dalton Trans.* 50 (1), 81–89. doi:10.1039/d0dt03057k
- Liu, J. Q., Luo, Z. D., Pan, Y., Kumar Singh, A., Trivedi, M., and Kumar, A. (2020). Recent developments in luminescent coordination polymers: designing strategies, sensing application and theoretical evidences. *Coord. Chem. Rev.* 406, 213145. doi:10.1016/j.ccr.2019.213145
- Long, J., Habib, F., Lin, P. H., Korobkov, I., Enright, G., Ungur, L., et al. (2011). Single-molecule magnet behavior for an antiferromagnetically superexchange-coupled dinuclear dysprosium(III) complex. *J. Am. Chem. Soc.* 133 (14), 5319–5328. doi:10.1021/ja109706y
- Lorenz, V., Fischer, A., and Edelmann, F. T. (2002). Silsesquioxane chemistry: Part 10. Silsesquioxane silanolate complexes of samarium and scandium. *J. Organomet. Chem.* 647 (1), 245–249. doi:10.1016/s0022-328x(01)01434-6
- Lorenz, V., Gießmann, S., Gun'ko, Y. K., Fischer, A. K., Gilje, J. W., and Edelmann, F. T. (2004). Fully metalated silsesquioxanes: building blocks for the construction of catalyst models. *Angew. Chem. Int. Ed.* 43 (35), 4603–4606. doi:10.1002/anie.200454094
- Lyubov, D. M., Neto, A. N. C., Fayoumi, A., Lyssenko, K. A., Korshunov, V. M., Taydakov, I. V., et al. (2022). Employing three-blade propeller lanthanide complexes as molecular luminescent thermometers: study of temperature sensing through a concerted experimental/theory approach. *J. Mater. Chem. C* 10 (18), 7176–7188. doi:10.1039/d2ct01289h
- Malkin, B. Z. (2005). “Ion-phonon interactions,” in *Spectroscopic properties of rare earths in optical materials*. Editors R. Hull, J. Parisi, R. M. Osgood, H. Warlimont, G. Liu, and B. Jacquier (Berlin, Heidelberg: Springer), 130–190. doi:10.1007/3-540-28209-2_3
- Malta, O. L. (2008). Mechanisms of non-radiative energy transfer involving lanthanide ions revisited. *J. Non-Crystalline Solids* 354 (42), 4770–4776. doi:10.1016/j.jnoncrysol.2008.04.023
- Manzur, J., Fuentealba, P., Gil, Y., Pérez-Obando, J., Morales Alfaro, J., Vega Carvallo, A. I., et al. (2023). Tuning the emission of homometallic Dy^{III} , Tb^{III} , and Eu^{III} 1-D coordination polymers with 2,6-di(1H-1,2,4-triazole-1-yl-methyl)-4-R-phenoxy ligands: sensitization through the singlet state. *Inorg. Chem.* 62 (47), 19195–19207. doi:10.1021/acs.inorgchem.3c02201
- Marchesi, S., Carniato, F., and Boccaleri, E. (2014). Synthesis and characterisation of a novel europium(III)-containing heptaisobutyl-POSS. *New J. Chem.* 38 (6), 2480–2485. doi:10.1039/c4nj00157e
- Miyakawa, T., and Dexter, D. L. (1970). Phonon sidebands, multiphonon relaxation of excited states, and phonon-assisted energy transfer between ions in solids. *Phys. Rev. B* 1 (7), 2961–2969. doi:10.1103/physrevb.1.2961
- Miyata, K., Hasegawa, Y., Kuramochi, Y., Nakagawa, T., Yokoo, T., and Kawai, T. (2009). Characteristic structures and photophysical properties of nine-coordinate europium(III) complexes with tandem-connected tridentate phosphine oxide ligands. *Eur. J. Inorg. Chem.* 2009 (32), 4777–4785. doi:10.1002/ejic.200900598
- Miyata, K., Nakanishi, T., Fushimi, K., and Hasegawa, Y. (2012). Solvent-dependent luminescence of eight-coordinated Eu(III) complexes with bidentate phosphine oxide. *J. Photochem. Photobiol. A Chem.* 235, 35–39. doi:10.1016/j.jphotochem.2012.03.005
- Monteiro, JHSC (2020). Recent advances in luminescence imaging of biological systems using lanthanide(III) luminescent complexes. *Molecules* 25 (9), 2089. doi:10.3390/molecules25092089
- Moos, H. W. (1970). Spectroscopic relaxation processes of rare earth ions in crystals. *J. Luminescence* 1-2, 106–121. doi:10.1016/0022-2313(70)90027-x
- Moura Jr., R. T., Carneiro Neto, A. N., Aguiar, E. C., Santos-Jr., C. V., de Lima, E. M., Faustino, W. M., et al. (2021b). (INVITED) JOYSpectra: a web platform for luminescence of lanthanides. *Opt. Mater. X* 11, 100080. doi:10.1016/j.omx.2021.100080
- Moura Jr., R. T., Oliveira, J. A., Santos, I. A., de Lima, E. M., Carlos, L. D., Aguiar, E. C., et al. (2021a). Theoretical evidence of the singlet predominance in the intramolecular energy transfer in Ruhemann's purple Tb(III) complexes. *Adv. Theory Simulations* 4 (3), 2000304. doi:10.1002/adts.202000304
- Nigoghossian, K., Kulakova, A. N., Félix, G., Khrustalev, V. N., Shubina, E. S., Long, J., et al. (2021). Temperature sensing in $\text{Tb}^{3+}/\text{Eu}^{3+}$ -based tetranuclear silsesquioxane cages with tunable emission. *RSC Adv.* 11 (55), 34735–34741. doi:10.1039/d1ra06755a
- Ning, Y., Zhu, M., and Zhang, J. L. (2019). Near-infrared (NIR) lanthanide molecular probes for bioimaging and biosensing. *Coord. Chem. Rev.* 399, 213028. doi:10.1016/j.ccr.2019.213028
- Pelluau, T., Sene, S., Ali, L. M. A., Félix, G., Neto, A. N. C., Carlos, L. D., et al. (2023). Hybrid multifunctionalized mesostructured stellate silica nanoparticles loaded with β -diketonate $\text{Tb}^{3+}/\text{Eu}^{3+}$ complexes as efficient ratiometric emissive thermometers working in water. *Nanoscale* 15, 14409–14422. doi:10.1039/d3nr01851b
- Prigyi, N., Channungkalakul, S., Ervithayasuporn, V., Yodsins, N., Jungstittiwong, S., Takeda, N., et al. (2019). Lithium-templated formation of polyhedral oligomeric silsesquioxanes (POSS). *Inorg. Chem.* 58 (22), 15110–15117. doi:10.1021/acs.inorgchem.9b01836
- Reisfeld, R., and Jørgensen, C. K. (1977). “Lasers and excited states of rare earths,” in *Inorganic chemistry concepts*. Editors M. Becke, M. F. Lippert, J. L. Margrave, R. W. Parry, C. K. Jørgensen, S. J. Lippard, et al. (Berlin, Heidelberg: Springer). doi:10.1007/978-3-642-66696-4
- Riseberg, L. A., and Weber, M. J., III (1977). “Relaxation phenomena in rare-earth luminescence,” in *Progress in optics*. Editor E. Wolf (Elsevier).
- Rocha, J., Brites, C. D. S., and Carlos, L. D. (2016). Lanthanide organic framework luminescent thermometers. *Chem. – A Eur. J.* 22 (42), 14782–14795. doi:10.1002/chem.201600860
- Rodríguez-Cortiñas, R., Avecilla, F., Platas-Iglesias, C., Imbert, D., Bünzli, J. C. G., de Blas, A., et al. (2002). Structural and photophysical properties of heterobimetallic 4F₇Zn iminophenolate cryptates. *Inorg. Chem.* 41 (21), 5336–5349. doi:10.1021/ic025587s
- SeethaLekshmi, S., Ramya, A. R., Reddy, M. L. P., and Varughese, S. (2017). Lanthanide complex-derived white-light emitting solids: a survey on design strategies. *J. Photochem. Photobiol. C Photochem. Rev.* 33, 109–131. doi:10.1016/j.jphotochemrev.2017.11.001
- Shchegolikina, O. I., Pozdniakova, Y. A., Lindeman, S. V., Zhdanov, A. A., Psaro, R., Ugo, R., et al. (1996). Cyclosiloxane sandwich complexes of a lanthanide metal: $\text{Na}_6\{[(\text{C}_6\text{H}_5\text{SiO}_2)_8]_2\text{Nd}_4(\mu_4\text{-O})\}$. *J. Organomet. Chem.* 514 (1), 29–35. doi:10.1016/0022-328x(95)06005-h
- Sheng, K., Si, W. D., Wang, R., Wang, W. Z., Dou, J., Gao, Z. Y., et al. (2022a). Keggin-type tridecanuclear europium-oxo nanocluster protected by silsesquioxanes. *Chem. Mater.* 34 (9), 4186–4194. doi:10.1021/acs.chemmater.2c00627
- Sheng, K., Wang, R., Bilyachenko, A., Khrustalev, V., Jagodić, M., Jagličić, Z., et al. (2022b). Tridecanuclear Gd(III)-silsesquioxane: synthesis, structure, and magnetic property. *Chem. Phys. Mater* 1 (4), 247–251. doi:10.1016/j.cphma.2022.04.008
- Suta, M., and Meijerink, A. (2020). A theoretical framework for ratiometric single ion luminescent thermometers—thermodynamic and kinetic guidelines for

optimized performance. *Adv. Theory Simulations* 3 (12), 2000176. doi:10.1002/adts.202000176

Suzuki, M., Tseeb, V., Oyama, K., and Ishiwata, S. (2007). Microscopic detection of thermogenesis in a single HeLa cell. *Biophysical J.* 92 (6), L46–L48. doi:10.1529/biophysj.106.098673

Trannoy, V., Carneiro Neto, A. N., Brites, C. D. S., Carlos, L. D., and Serier-Brault, H. (2021). Engineering of mixed $\text{Eu}^{3+}/\text{Tb}^{3+}$ metal-organic frameworks luminescent thermometers with tunable sensitivity. *Adv. Opt. Mater.* 9 (6), 2001938. doi:10.1002/adom.202001938

Wang, J., Deng, R., MacDonald, M. A., Chen, B., Yuan, J., Wang, F., et al. (2014). Enhancing multiphoton upconversion through energy clustering at sublattice level. *Nat. Mater.* févr 13 (2), 157–162. doi:10.1038/nmat3804

Wu, G., Chen, Y., Xu, D. J., Liu, J. C., Sun, W., and Shen, Z. (2009). Synthesis and molecular structure of a tetrameric neodymium-silsesquioxane cage complex: $\{[(i\text{-C}_4\text{H}_9)_7(\text{Si}_7\text{O}_{12})\text{Nd}]_4\text{NaCl}\}$. *J. Organomet. Chem.* 694 (9), 1571–1574. doi:10.1016/j.jorganchem.2009.01.042

Yanagisawa, K., Nakanishi, T., Kitagawa, Y., Seki, T., Akama, T., Kobayashi, M., et al. (2015). Seven-coordinate luminophores: brilliant luminescence of lanthanide complexes with C_{3v} geometrical structures. *Eur. J. Inorg. Chem.* 2015 (28), 4769–4774. doi:10.1002/ejic.201500820

Yang, C., Fu, L. M., Wang, Y., Zhang, J. P., Wong, W. T., Ai, X. C., et al. (2004). A highly luminescent europium complex showing visible-light-sensitized red emission: direct observation of the singlet pathway. *Angew. Chem. Int. Ed.* 43 (38), 5010–5013. doi:10.1002/anie.200454141